Interfacial oxygen vacancy modulated Ag$_3$PO$_4$ @MoS$_2$ Z-scheme system for efficient photocatalytic hydrogen recovery from antibiotic wastewater

Shuqu Zhang , Guanghua Hu , Meixue Chen , Bing Li , Weili Dai , Fang Deng , Lixia Yang [*] , Jianping Zou , Shenglian Luo

Key Laboratory of Jiangxi Province for Persistent Pollutants Control and Resources Recycle, Nanchang Hangkong University, Nanchang 330063, Jiangxi Province, People's Republic of China

ABSTRACT

Z-scheme Ag$_3$PO$_4$ @MoS$_2$ photocatalyst was constructed by decorating MoS$_2$ nanosheets on Ag$_3$PO$_4$ cubes for recovering hydrogen energy from antibiotic wastewater. Abundant oxygen vacancies (Vo) distributed along with Ag$_3$PO$_4$ cube surface are responsible for MoS$_2$ lattice distortion by enabling 2 H phase MoS$_2$ around Vo partially transform in 1 T phase. Free radicals trapping and theoretical calculation approve that Vo act as intermediate medium of charge transferring in Z-scheme Ag$_3$PO$_4$ @MoS$_2$ system. On the strength of Vo and mixed phase of MoS$_2$ providing more exposed active sites, superior conductivity and excellent stability, photocatalytic hydrogen recovery over Ag$_3$PO$_4$ @MoS$_2$ is high up to 54.01 μmol·g^{-1}·h^{-1} from norfloxacin wastewater (degradation efficiency: 88.36%). It is found that bandgap matching between antibiotics molecule and Ag$_3$PO$_4$ @MoS$_2$ accounts for hydrogen recovery kinetics. H protons could be donated in the process of decyclopropylaton, dihydroxylation and demethylation for antibiotic degradation. This work presents new lines for seeking greater sustainability by managing antibiotics wastewater resource.

1. Introduction

With the development of industrialization and urbanization, water environmental pollution issues are becoming increasingly prominent and serious. Among water pollutants, antibiotics have been widely concerned, which have ecological toxicity for aquatic organisms due to the residuals in the environment [1]. Nowadays, as the concepts about resourcefulness of waste develops, wastewater is considered as a precious resource for containing a wealth of energy substances (like hydrogen) in the process of seeking the greatest sustainability of wastewater resource [2,3]. Therefore, it is necessary to explore new and green technology to eliminate the hazardous influence of antibiotics and extract energy from antibiotic wastewater to achieve nontoxic and resource-oriented strategies for wastewater managements.

Solar energy is generally accepted as an abundant, endless, and renewable energy source that may meet the current and future energy needs of human being [4,5]. In recent years, the mechanism of photocatalytic technology in wastewater purification and energy conversion has been well developed, and it shows bright application prospects in the field of wastewater utilization. It has been found that some organic pollutants can donate electrons, which have been used as sacrificial agents in the photocatalytic reduction process. Some semiconductor photocatalytic composites can degrade organic pollutants, obtaining certain amount of H$_2$ simultaneously [6]. Although the efficiency of H$_2$ production in photocatalytic water splitting is mainly limited by the four-electron kinetic process of O$_2$ production, it can be significantly engineered by converting the four-electron process of O$_2$ production to the two-electron process of H$_2$O$_2$/•OH with powerful catalysts [7,8]. For instance, Zhang et al. synthesized a MoS$_2$ quantum dot-decorated 3D nanoarchitecture (MoS$_2$QDs) of ZnIn$_2$S$_4$ and reduced grapheme oxide (MoS$_2$QDs@ZnIn$_2$S$_4$ @RGO) photocatalyst. It showed excellent H$_2$ production (H$_2$ amount: 45 μmol) during Rhodamine B (RhB) degradation (degradation efficiency: 98.8%) [9]. Stylianou et al. used RhB to replace the electron donor, with the aim of integrating the photocatalytic H$_2$ generation with the RhB degradation in one process [10]. However, it is difficult to maintain excellent performance and stability persistently in the process of photocatalytic wastewater purification with simultaneous hydrogen production. In order to solve those problems, some strategies have been reported to optimize the basal and interfacial structure of photocatalyst systems, including vacancy

engineering [11], interface engineering [12] and Z-scheme system, *etc.* [13,14]. Z-scheme systems have been extensively studied and used for photocatalytic application due to the unique way of transferring electrons to maintain high reducibility and superior oxidizing capacity synchronously [15,16]. Therefore, with unique Z-scheme photocatalysts, it is promising to achieve excellent photocatalytic hydrogen recovery from antibiotics wastewater [17].

Although many important discoveries have been presented, it is still desirable to construct a Z-scheme system with higher efficiency and activity to meet the demands of practical applications. Ag_3PO_4 photocatalysts have attracted considerable attentions due to their excellent visible-light-driven photocatalytic activity for the degradation of organic pollutants [18], which activity can be further improved through reconstructing the shape, morphology and crystal face of Ag_3PO_4 crystals [19]. However, Ag_3PO_4 is unstable under prolonged irradiation because of the photo-corrosion by the photogenerated electrons, leading to the serious structural damage and the unsatisfactory photocatalytic performance [20]. In order to improve the stability, constructing Ag_3PO_4-based photocatalyst composites with proper band matching can facilitate electron transfer to suppress the recombination of photo-generated carriers [21]. Molybdenum disulfide (MoS_2) as a cocatalyst for hydrogen evolution reaction (HER) can compete with the noble metal Pt and work as the substitute [22]. Besides, it has a graphene-like layered structure that exhibits a large specific surface area, which is conducive to gather organic pollutants [23,24]. It is reported that MoS_2 has the excellent character of toxic tolerance for organic pollutants [25]. What is more, 1 T-MoS_2 has better hydrogen production performance than 2 H-MoS_2 on account of the increased active sites on both basal plane and edges [26]. However, the metastable 1 T-MoS_2 tends to convert in the more stable 2 H-MoS_2, resulting in declined HER performance. It is necessary to explore wise strategy to stabilize 1 T-MoS_2 to attain exceptional and stable HER performance [27].

In this work, a novel and hierarchical Z-scheme Ag_3PO_4 @MoS_2 was constructed accurately for recovering hydrogen from antibiotic wastewater under irradiation. The MoS_2 nanosheets decorated on entire crystal planes {100} of Ag_3PO_4 cube act as protective coating to inhibit the photo-corrosion of Ag_3PO_4 cube. Rich oxygen vacancies (Vo) confined into Ag_3PO_4 could stabilize the distorted 1 T MoS_2, which also acted as interfacial recombination sites of Z-scheme Ag_3PO_4 @MoS_2, realizing the antibiotics elimination. Of note, the optimized Z-scheme Ag_3PO_4 @MoS_2 showed the outstanding photocatalytic activity for extracting hydrogen energy from antibiotics wastewater and maintained the excellent stability. The mechanism of antibiotics degradation and synergistic hydrogen production was discussed and uncovered in depth.

2. Experimental

2.1. Materials

Silver nitrate ($AgNO_3$), disodium hydrogen phosphate (Na_2HPO_4), aqueous ammonia ($NH_3 \cdot H_2O$), sodium molybdate (Na_2MoO_4), and thioacetamide (TAA) were obtained from Sinopharm Chemical Reagent Co., Ltd. (China). All chemicals were used without further purified in the experiments.

2.2. Synthesis of Ag_3PO_4 cubes (Ag_3PO_4-C) and Ag_3PO_4 @MoS_2 (AM)

The Ag_3PO_4 cubes (Ag_3PO_4-C) were prepared by using a direct precipitation approach. In a typical synthesis, $AgNO_3$ (0.3 g) was solved in deionized water (40 mL). Ammonia aqueous solution (0.1 M) was slowly added in the above solution under stirring. After solution became transparent, Na_2HPO_4 aqueous solution (8 mL, 0.15 M) was added in under vigorous stirring to generate Ag_3PO_4. Afterwards, the prepared Ag_3PO_4 cubes were washed with ethanol and deionized water several times and then dried at 60 °C. For comparison, irregular Ag_3PO_4

(Ag_3PO_4-I) particles were synthesized under the same conditions without ammonia.

The Ag_3PO_4 @MoS_2 (AM) was prepared via in-situ hydrothermal method. Sodium molybdate (Na_2MoO_4) and thioacetamide (C_2H_5NS) were dissolved in deionized water (20 mL) under stir to form Solution A. Meanwhile, the prepared Ag_3PO_4 cube powder (0.04 g) was dispersed in deionized water (20 mL) to form Solution B. Mixed Solution B with Solution A and transferred the mixture solution into a Teflon-lined stainless steel autoclave for a 24 h-heat treatment at 200 °C (Anhui Kemi Machinery Technology., LTD, China). The target product was obtained after centrifugation and dried at 60 °C. AM with different MoS_2 contents including 10, 12, 13, 14 and 15 wt% of MoS_2 were also synthesized in the same way by tailoring the amounts of Na_2MoO_4 (0.0101 g, 0.0121 g, 0.0131 g, 0.0141 g and 0.0152 g) and C_2H_5NS (0.0202 g, 0.0242 g, 0.0262 g, 0.0282 g and 0.0304 g). The prepared different composites were labeled as AM-x (x = 10, 12, 13, 14 and 15), respectively. For comparison, pure MoS_2 nanosheets were synthesized under the same conditions without adding Ag_3PO_4.

2.3. Characterizations

Scanning electron microscopy (SEM, Hitachi S-4800) was used to analyze the morphological structures of all the photocatalyst samples. The finely detailed microstructures were observed at 200 kV using transmission electron microscopy (TEM, JEOL, JEM-2100 F (HR)). Using X-ray diffraction (XRD, Bruker, Germany), the crystal phases of materials were identified. The electronic structures and chemical states of elements measured by X-ray photoelectron spectroscopy (XPS) measurements were acquired with a VG Escalab 250 spectrometer equipped with an Al anode. At room temperature, the photoluminescence (PL) spectra were measured using a fluorescence spectrophotometer (Hitachi F4500). A fluorescence spectrophotometer (EDINBURGH FS5) with an excitation wavelength of 380 nm was used to record the fluorescence emission spectra. An electrochemical workstation with a three-electrode electro-chemical system (Chenhua Instrument Co., Shanghai) was used to conduct photocurrent responses. As the reference electrode, counter electrode and working electrode, respectively, we employed an Ag/AgCl electrode, a Pt electrode and fluoride tin oxide (FTO) with covered as-prepared samples (active area of 1.0×1.0 cm^2) in Na_2SO_4 aqueous solution (0.2 M, pH = 6.8). Using a spectrometer (Bruker EMXplus-6/1) at room temperature, the EPR measurements were made. An integrating sphere-equipped UV–vis spectrophotometer (Cary 300) was used to capture the diffuse reflection spectra (DRS) in the UV–vis range. Total Organic Carbon (TOC) was measured using a TOC analyzer (TOC-L CPH/CPN, Shimadzu, Japan). The degradation intermediate products were analyzed using liquid chromatography mass spectrometry (LC-MS) (Ultimate 3000 UHPLC -Q Exactive).

2.4. Evaluation of photocatalytic performance

Photocatalytic degradation of ciprofloxacin: The photocatalytic degradation of ciprofloxacin was used to assess the photocatalytic performance of Ag_3PO_4 and AM-x (x = 10, 12, 13, 14, and 15) composites. 30 mg photocatalyst was dispersed into ciprofloxacin solution (100 mL, 10 mg/L) and sonicated for 2 mins. In order to achieve complete adsorption-desorption equilibrium, continuous stirring was performed for 30 min under dark conditions. Following that, the reaction mixture was exposed to a 300 W xenon arc lamp (PLS-SXE 300 C, Perfect light, China). 3 mL solution samples were withdrawn intermittently for 15 mins, and filtered through a 0.22 μm Millipore filter to remove the particles and analyzed with a UV–vis spectrophotometer (Hitachi, U-3900 H). Free radical capture experiment: 3.6 μL isopropanol (IPA), 3.6 μL 1, 4-benzoquinone (BQ), and 3 mg ethylenedia-minetetraacetic acid disodium (EDTA-2Na) were respectively added to ciprofloxacin solution (100 mL, 10 mg/L) dispersed with 30 mg of photocatalyst. After sonication for 2 mins, the obtained solution was stirred continuously under

dark conditions for 30 mins and then continuously under light conditions for 2 h. 3 mL sample was taken before and after the reaction and analyzed by UV-*vis* spectrophotometer. The experimental conditions of the radical burst experiment were the same as those of the photocatalytic degradation of ciprofloxacin.

Photocatalytic H_2 recovery from antibiotics wastewater: The photocatalytic performance of the prepared catalyst for H_2 recovery from antibiotics wastewater was evaluated in a Labsolar-6A closed gas system (Beijing Perfectlight, China). In a typical experiment, 30 mg of AM-13 photocatalyst was dispersed in antibiotics solution (ciprofloxacin (CIP), tetracycline hydrochloride (TC), ofloxacin (OFL) and norfloxacin (NOR): 100 mL, 10 mg/L). Before illumination, the suspension was vacuumed to remove the dissolved air. Then, the photocatalytic experiments were carried out in a circulating water system at 6 °C under the illumination of a 300 W xenon lamp. The generated hydrogen was determined by online gas chromatography (FLGC9790II, TCD).

2.5. Theoretical calculation

All density generalized function theory (DFT) calculations were performed using the PBE formulation in the generalized gradient approximation (GGA) using the Vienna Ab Initio Package (VASP) [28, 29]. The projection enhanced wave (PAW) potential was chosen to describe the ion nuclei and the valence electrons were considered using a plane wave basis set with a kinetic energy cutoff of 450 eV [30]. The use of Gaussian smearing and a width of 0.05 eV allowed for partial occupancy of the Kohn-Sham orbitals. When the energy change was less than 10^{-4} eV, the electron energy was assumed to be self-consistent. When the force variation was less than 0.05 eV/Å, a geometry optimization was deemed to have reached convergence. The dispersion interactions were characterized by the DFT-D3 approach of Grimme. The surfaces structures of the $2 \times 2 \times 1$ monkhorst pack K-point sampling are employed for the Brillouin zone integral.

The oxygen vacancy formation energy (E_{vo}) is described as follows:

$$E_{vo} = E_{def} - E_{bulk} + 1/2E_{O2}$$

where E_{def} is the system energy with a loss of one oxygen atom (O), E_{bulk} is the energy of a slab without the loss of an oxygen atom, and E_{O2} is the energy of an O_2 molecule in the gas phase.
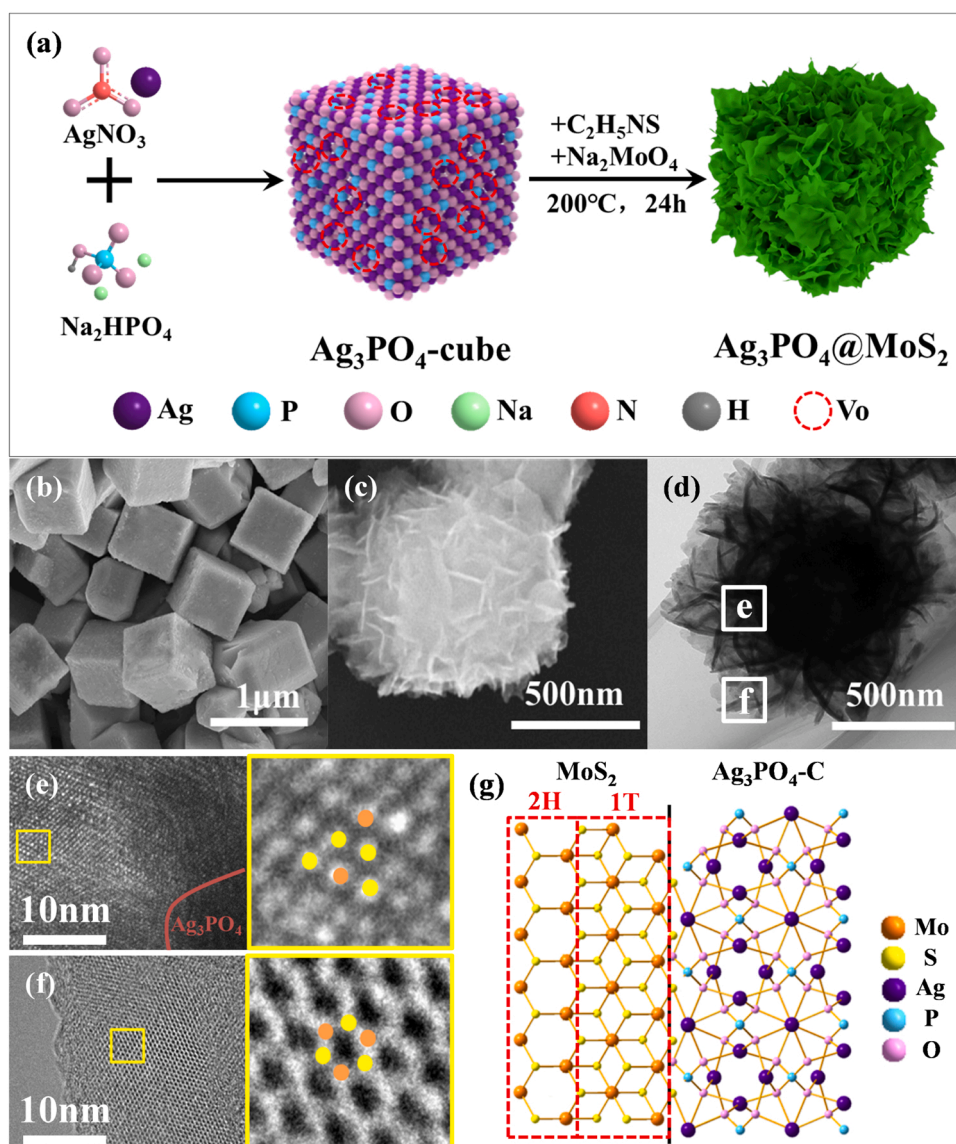
Fig. 1. (a) Schematic illustration of the synthetic procedure of AM. (b) SEM image of Ag_3PO_4 cubes. (c) SEM image and (d) TEM image of AM-13. HRTEM image of (e) AM-13 and (f) MoS_2. (g) The corresponding atomic model for phase comparison of MoS_2 at the interface between Ag_3PO_4-C and MoS_2.

3. Results and discussion

3.1. Structural characterization of Ag₃PO₄ @MoS₂ composites

The synthetic procedure of the composite photocatalyst Ag_3PO_4 @MoS₂ (AM) was depicted in Fig. 1a. Ag_3PO_4 cubes (Ag_3PO_4-C) with oxygen vacancies (Vo) enriching surface was synthesized using $AgNO_3$ and Na_2HPO_4 as precursors and NH_3 as pH regulator and capping agent [31]. MoS₂ nanosheets were in-situ grown on the Ag_3PO_4-C. SEM image of Ag_3PO_4-C (Fig. 1b) show the Ag_3PO_4-C have smooth surface and regularly cubic construction. For comparison, the SEM of the synthesized irregular Ag_3PO_4 (Ag_3PO_4-I) is shown in Fig. S1a, presenting irregular nanoparticles. In addition, the SEM images of MoS₂ and catalysts with different proportions are exhibited in Fig. S1b-f. The SEM and TEM images of AM-13 were given in Fig. 1c and d, demonstrating the uniform loading of MoS₂ nanosheets on Ag_3PO_4-C. The elemental mapping of a single AM cube using energy-dispersive X-ray spectroscopy (EDX) shows that the Ag, P, O, Mo, and S elements are uniformly distributed (Fig. S2), suggesting that the MoS₂ nanosheets wrap Ag_3PO_4 cube. Numerous MoS₂ nanosheets are densely assembled along the Ag_3PO_4 cube surface. building a heterojunction. HRTEM images (Fig. 1e and f) show that 1 T and 2 H phase of MoS₂ grow together respectively. 1 T phase is observable near the interface of Ag_3PO_4 @MoS₂ and 2 H phase at the MoS₂ edge. The corresponding atomic model of for phase comparison of MoS₂ at the interface between Ag_3PO_4-C and MoS₂ was shown in Fig. 1g. MoS₂ nanosheets presents the 1 T phase near the interface, while 2 H phase far away from the interface, which is miscible for 2 H and 1 T phase (1 T&2 H-MoS₂). It is reported the MoS₂ with mixed 1 T-2 H phase structure displays significantly enhanced hydrogen evolution due to its highly exposed active sites and superior conductivity [32].

3.2. Characterization of oxygen vacancies and 1 T phase MoS₂

The elemental composition and chemical states of the Ag_3PO_4-C, Ag_3PO_4-I, MoS₂ and AM-13 were further analyzed by XPS to inspect the surface and interface properties. Fig. S3 shows the full XPS spectrum of MoS₂, Ag_3PO_4-C and AM-13, which exhibits Ag, P, O, Mo and S peaks. No peaks corresponding to impurity are observed. Fig. 2a-c show the XPS peak of Ag 3d, P 2p and O 1 s of AM-13 Ag_3PO_4-C and Ag_3PO_4-I. The Ag 3d spectrum of the Ag_3PO_4-I is deconvoluted in two individual peaks at 368.24 eV and 374.27 eV, which are indexed to the Ag 3d$_{5/2}$ and Ag 3d$_{3/2}$ respectively [33]. For Ag_3PO_4-C, the specific peaks of Ag 3d$_{5/2}$ and Ag 3d$_{3/2}$ shift to 368.29 eV and 374.33 eV because of the exposure for crystal facet {100} with high energy (shown in Fig. S4). The XPS peaks of P 2p and O 1 s in Ag_3PO_4-I locate at 133.33 eV and 531.89 eV, respectively. The XPS peak of P 2p positively shifts to 133.35 eV and O 1 s of Ag_3PO_4-C negatively shifted to 530.89 eV. The decreased binding energy (BE) of O 1 s for Ag_3PO_4-C may be caused by Vo on the Ag_3PO_4-C surface for Vo working as centers for trapping electrons, which increases the electron density of O atoms nearby [34]. EPR spectra of Ag_3PO_4-C and Ag_3PO_4-I were collected to further identify the Vo existence, as shown in Fig. 2d. Ag_3PO_4-C shows intense signal at g ≈ 2.001, which is associated with the presence of Vo [35]. The AM photocatalyst showed the reduced oxygen vacancies by combining with MoS₂. It strongly indicated that oxygen vacancies could be regulated by sewing and filling of different MoS₂ contents. Eventually, interfacial oxygen vacancies modulated intimate and compact interface are formed, which is beneficial for efficient electrons migration [36,37]. Besides, the formation energy of Vo is 0.53 eV for Ag_3PO_4-C, and 1.03 eV for Ag_3PO_4-I, as depicted in Fig. S5. It indicates that Vo on the surface of Ag_3PO_4-C is easier to be formed than that on Ag_3PO_4-I.

With MoS₂ nanosheets decorated, the XPS peaks of Ag, P, O in AM-13

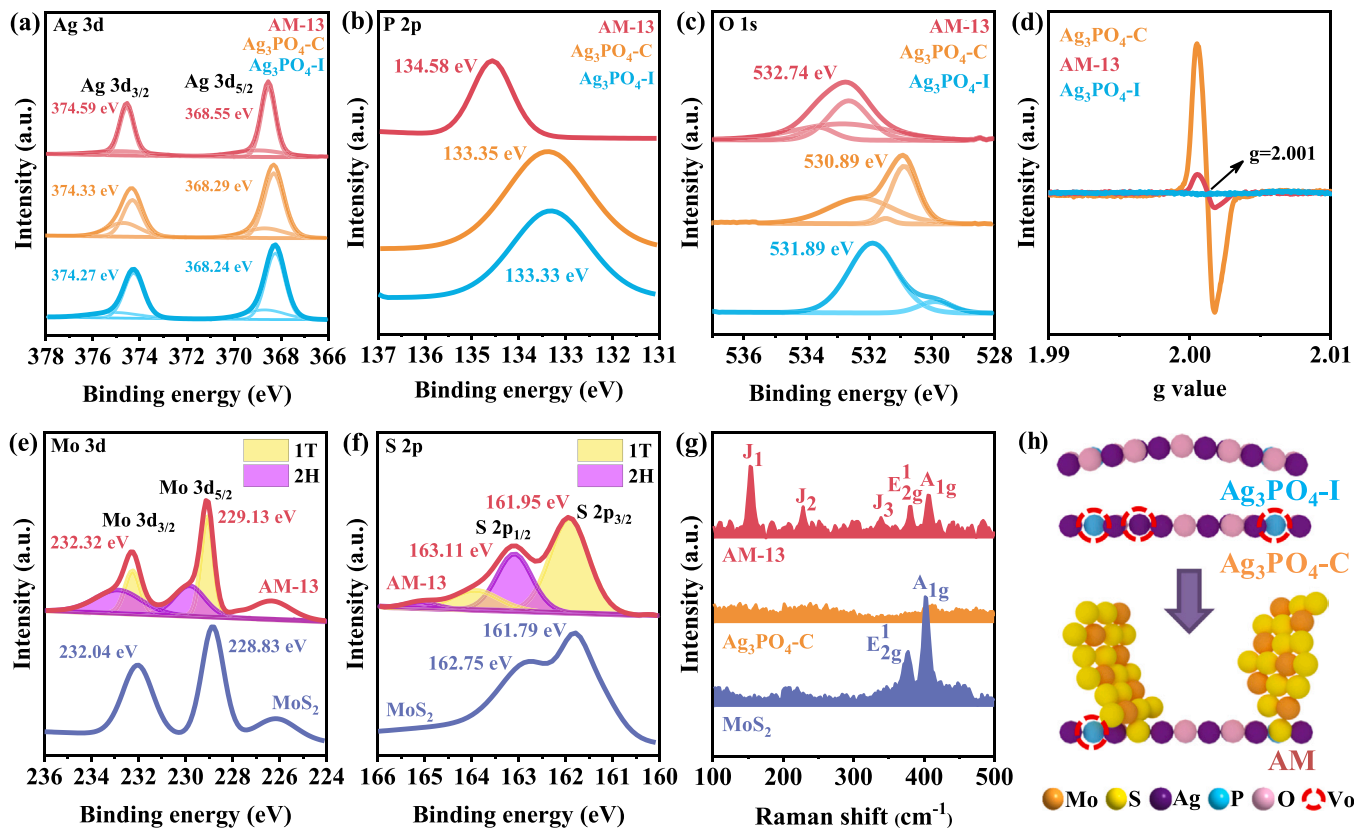**Fig. 2.** High-resolution XPS spectra of (a) Ag 3d, (b) P 2p, (c) O 1 s over Ag_3PO_4-I, Ag_3PO_4-C and AM-13. (d) EPR spectra of Vo in Ag_3PO_4-I, Ag_3PO_4-C and AM-13. High-resolution XPS spectra of (e) Mo 3d and (f) S 2p over MoS₂ and AM-13. (g) Raman spectra of AM-13, Ag_3PO_4-C and MoS₂. (h) The diagram of the surface of Ag_3PO_4-I, Ag_3PO_4-C and AM.

positively shift relative to Ag_3PO_4-C, as the binding energies of Ag $3d_{5/2}$ and Ag $3d_{3/2}$ are both increased by 0.26 eV, the P 2p peaks shift from 133.35 eV to 134.58 eV, and the O 1 s peaks shift from 530.89 eV to 532.74 eV (Fig. 2a-c). All the shifts of Ag, P and O elements might be attributed to the powerful electronic interaction between MoS_2 and Ag_3PO_4-C. In Fig. 2e, the peaks of Mo^{4+} of pure MoS_2 located at 228.83 eV and 232.04 eV are corresponded to the Mo $3d_{5/2}$ and Mo $3d_{3/2}$ peaks, respectively. These two peaks are divided into four peaks at 229.10 and 232.28 eV, 229.88 and 232.92 eV, which are associated with 1 T- and 2 H-MoS_2 respectively. As depicted in Fig. 2f, the peak located at 161.79 eV and 162.75 eV are pertained to S $2p_{3/2}$ and S $2p_{1/2}$, which are also deconvolved into four peaks containing those at 161.93 and 163.94 eV (1 T-MoS_2), and 163.09 and 165.09 eV (2 H-MoS_2). It is shown that the binding energy of the core-level electrons of Mo^{4+} and S^{2-} in MoS_2 are affected after combined with Ag_3PO_4-C [38]. Notably, the rich Vo on the Ag_3PO_4-C surface can be sewed mostly by MoS_2 nanosheets (Fig. 2d). It could be calculated that Vo confined on the Ag_3PO_4-C surface are responsible for the 1 T-MoS_2 formation. Raman spectra are used to delve deeper into the phase characteristics of MoS_2. Fig. 2g shows that synthesized MoS_2 possesses the representative peaks of 2 H-MoS_2, which are assigned to the E_{2g}^1 and A_{1g} modes [39]. The reverse vibration of the two S atoms with respect to Mo between them produce rise to the in-plane mode E_{2g}^1, while the A_{1g} mode is ascribed to the out-of-plane vibration of the S atoms in the reverse direction. The E_{2g}^1 and the A_{1g} of AM-13 are blue-shifted compared to MoS_2 (E_{2g}^1 shifts from 377 to 380 cm^{-1} and A_{1g} shifts from 403 to 407 cm^{-1}). This might be the changed original vibration mode of the Mo-S bonds due to the interaction with the S layer of MoS_2 and Ag_3PO_4-C [40]. The characteristic peaks of J_1 (154 cm^{-1}), J_2 (228 cm^{-1}) and J_3 (339 cm^{-1}) originated from the S-Mo-S band of 1 T-MoS_2 appear in the spectrum of AM-13, which demonstrates that the synthesized MoS_2 is composed of 2 H and 1 T phases with a few-/mono-layer structure [41]. Fig. 2g shows the schematic illustration for the surface Ag_3PO_4-I and Ag_3PO_4-C, and the interface between MoS_2 and Ag_3PO_4-C. Surface Vo on the Ag_3PO_4-C modulates the distortion and phase transformation of 2 H-MoS_2,

resulting in the mixed phase structure of MoS_2 in Ag_3PO_4 @MoS_2.

3.3. Photoelectrical properties and photocatalytic performance for Ag_3PO_4 @MoS_2 composites when degrading ciprofloxacin

The photoluminescence (PL) emission spectra of Ag_3PO_4-C and those AM composites with various MoS_2 loading contents were recorded to determine the separation rate of photogenerated carriers, which is vital to the catalytic activity. PL spectra excited at 365 nm of Ag_3PO_4-C and different AM composites are shown in Fig. 3a. As shown, the relative intensity of the emission spectra of Ag_3PO_4-C is the highest. It means that photogenerated carriers of Ag_3PO_4-C are easier to recombine, resulting in unexpected photo-corrosion [42]. The relative intensity of all the AMs is lower than that of Ag_3PO_4-C, implying that MoS_2 coating can inhibit the photo-corrosion of Ag_3PO_4-C by accelerating the separation of photogenerated carriers. AM-13 demonstrates the minimum PL intensity, indicating the most appropriate conjugation between Ag_3PO_4 and MoS_2. Time-resolved transient photoluminescence (TRPL) analysis was carried out to investigate migration dynamics of photoinduced carriers, with results exhibited in Fig. 3b. The reduced lifetime of photoexcited charges is associated with facilitated electron transport. AM-13 shows shorter fluorescence lifetime than that of Ag_3PO_4-C, which suggests that the MoS_2 effectively restrains the combination of photogenerated electron-hole pairs [43–47]. The photocurrents responses (Fig. 3c) of Ag_3PO_4-C, MoS_2 and AM-13 were recorded to reveal the migration behavior and separation of charges carriers. AM-13 demonstrates the highest photocurrent, indicating that remarkable efficiency in photocatalysis will be achieved there. All in all, The AM-13 photocatalyst showed the best photoelectric properties, which may present the excellent photocatalytic performance.

The photocatalytic performance of decomposing ciprofloxacin (CIP) was assessed over Ag_3PO_4-C and AM composites. The influence of pH and CIP concentration for degradation efficiency was investigated, corresponding results are depicted in Fig. S6 [48]. It is found that the photocatalytic degrading CIP show better performance at lower pH and
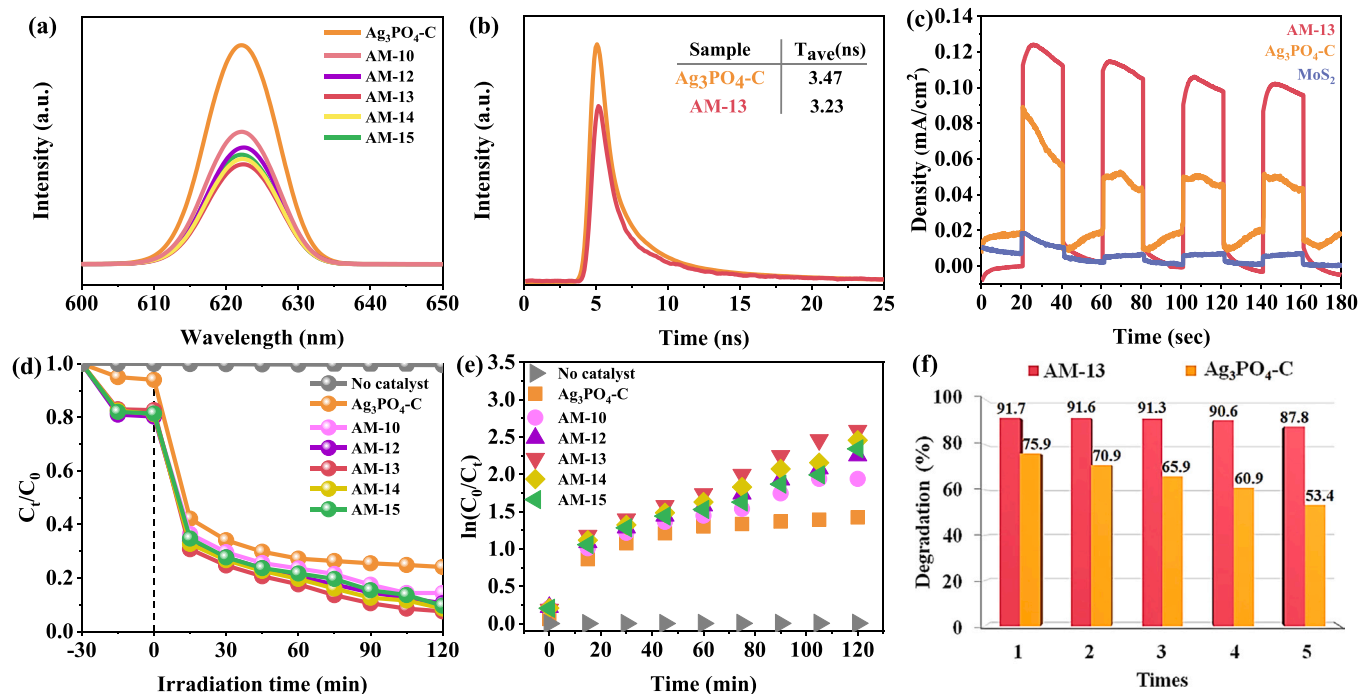
Fig. 3. (a) PL spectra of Ag_3PO_4-C and as-prepared different AM composites. (b) TRPL decay spectra of Ag_3PO_4-C and AM-13. (c) Photocurrent responses of AM-13, Ag_3PO_4-C and MoS_2. (e) Kinetic curves for the CIP degradation over as-prepared photocatalysts.
(a) (d) Photodegradation curves of CIP over as-prepared photocatalyst (CIP concentration: 10 mg/L, pH = 5, light source: λ = 280–780 nm). (b) (f) Recycling photocatalytic tests for CIP degradation over AM-13 and Ag_3PO_4-C (CIP concentration: 10 mg/L, pH = 5, light source: λ = 280–780 nm).

low initial concentration. The performance evolution of all the photo-catalysts was conducted at pH = 5 and 10 mg/L concentration (Fig. 3d). After reaching adsorption equilibrium at 30 min, the removal efficiency of CIP rendered by Ag_3PO_4-C is 75.9% within 120 min, which is promoted to 91.7% with AM-13, the best removal efficiency. On the one hand, insufficient MoS_2 content shows the powerless and weak transferring efficiency for photogenerated carriers between interfaces and will not prevent Ag_3PO_4-C from photo-corrosion effectively. On the other hand, excessive MoS_2 content may lead to the stacking of MoS_2 nanosheets loaded on the surface of Ag_3PO_4-C, which resist the light utilization and affect the 1 T phase stability. The corresponding kinetic

curves (Fig. 3e) follow the pseudo-first-order reaction model [49]. The stability and reusability of Ag_3PO_4-C and AM-13 for degrading CIP were evaluated through repeated runs (Fig. 3f and Fig. S7). After five cycles, the photocatalytic efficiency of degrading CIP over Ag_3PO_4-C and AM-13 decreases by 22.5% and 3.9%, respectively. It is posited that the MoS_2 surface coating suppresses the Ag_3PO_4 photo-corrosion by reducing light sensitivity and promoting photogenerated carrier separation. Besides, the used AM-13 maintains the original three-dimensional hierarchitectures with MoS_2 edge still exposed and distorted (Fig. S8), validating its structural stability. Moreover, the stability of 1 T-MoS_2 in used AM-13 (Fig. S9) was studied with XPS
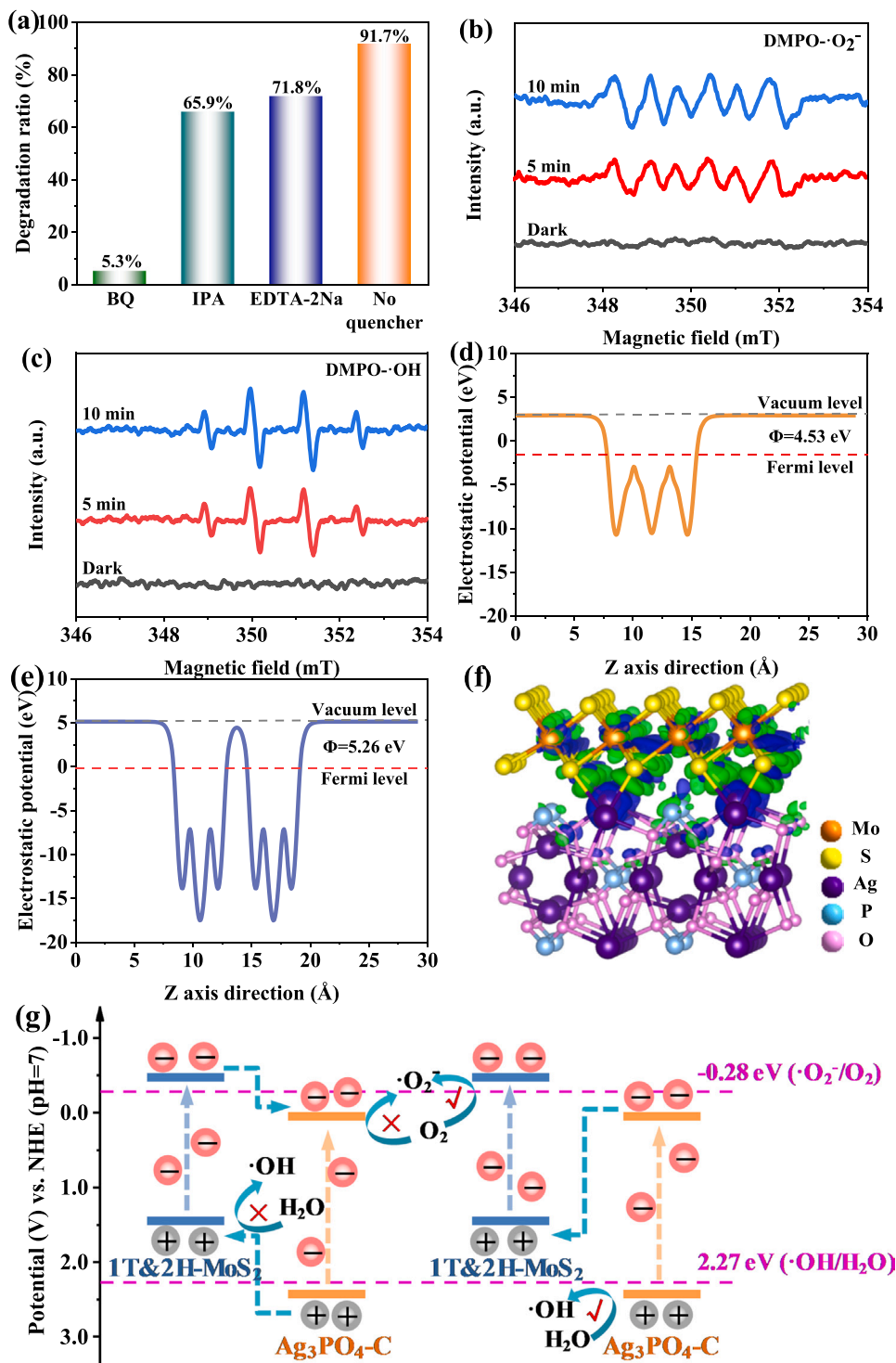
Fig. 4. (a) Degradation efficiency of CIP over AM-13 in presence of different radical quenchers. DMPO spin-rapping EPR spectra of (b) DMPO-•O_2 and (c) DMPO-•OH on AM-13. Electrostatic potentials of simulated models of (d) Ag_3PO_4-C and (e) MoS_2. (f) The planar averaged charge density difference for the AM model, the blue and green region represents the consumption and accumulation of electrons. (g) Schematic illustration of transfer behavior of carriers by following the Z-Scheme construction in AM composites.

spectra. Compared with fresh AM-13, the full spectrum and high-resolution XPS spectra of different elements in used AM-13 slightly shift. The unchanged proportion of 1 T and 2 H-MoS$_2$ in Mo 3d and S 2p show that 1 T-MoS$_2$ stably anchors on AM-13 after the cyclic reaction [50]. Above findings manifest that Vo enriched Ag$_3$PO$_4$-C reinforces the stable implantation of 1 T- and 2 H-MoS$_2$ in Ag$_3$PO$_4$ substrate, realizing the outstanding photocatalytic performance and stability for CIP degradation.

3.4. Mechanism identification for Z-Scheme Ag$_3$PO$_4$ @MoS$_2$ system

The mechanism of AM photocatalyst system with high activity and stability in CIP degradation is expounded based on free radical trapping and theoretical calculation. To determine the roles of involved radicals, ethylenedia-minetetraacetic acid disodium (EDTA-2Na), isopropanol (IPA) and 1, 4-benzoquinone (BQ) are adopted as scavengers for h^+, •OH and •O$_2^-$, respectively [51]. Fig. 4a shows the CIP degradation efficiency over AM-13 with different radical quenchers. The CIP degradation is significantly depressed in the presence of BQ, indicating •O$_2^-$ is the pivotal active species. The electron paramagnetic resonance (EPR) test was carried out to further affirm the generation of •O$_2^-$ and •OH species in AM photocatalyst system. Four specific peaks assigned to DMPO− •O$_2^-$ are displayed in Fig. 4b, their signal intensity enhances with the increased irradiation time. And no signal was detected in the darkness. EPR spectra of DMPO− •OH exhibit the same trend (Fig. 4c). The free radical trapping and EPR spectra demonstrates that Ag$_3$PO$_4$-C@MoS$_2$ photocatalyst systems hold the excellent oxidation and reduction properties [52].

The bandgap structure of Ag$_3$PO$_4$-C@MoS$_2$ was analyzed to elucidate its influence on the photocatalytic activity. In Fig. S10a, the UV-*vis* diffuse reflectance spectra (DRS) of Ag$_3$PO$_4$, MoS$_2$, Ag$_3$PO$_4$ @MoS$_2$ with variable ingredient ratio are illustrated. The Ag$_3$PO$_4$ @MoS$_2$ composites show a wider absorption in the visible light region than individual Ag$_3$PO$_4$, MoS$_2$. Based on transformed Kubelka–Munk function (Fig. S10b), the bandgap value of Ag$_3$PO$_4$-C and MoS$_2$ is 2.37 eV and 1.93 eV, respectively [53]. The conduction bands (CBs)/valence bands (VBs) for Ag$_3$PO$_4$-C and MoS$_2$ are computed and evaluated by XPS (Fig. S10c and d), which are 0.06/2.43 eV and − 0.49/1.44 eV, respectively (Fig. S10e). Fermi level is an important indicator for estimating the charge transport on the catalyst surface, which can be obtained from the formula: $\Phi = E_{va} - E_f$, where Φ is work function, E_{va} vacuum level, and E_f represents fermi level. The electrostatic potentials of Ag$_3$PO$_4$-C and 2 H-MoS$_2$ are shown in Fig. 4d and e, and their calculated work functions are 4.53 eV and 5.26 eV, respectively. As E_f of 2 H-MoS$_2$ (−0.12 eV) is greater than that of Ag$_3$PO$_4$-C (−1.58 eV), driven by the potential difference, the electrons transfer from Ag$_3$PO$_4$-C to 2 H-MoS$_2$ until the Fermi levels reach equilibrium in Fig. S11 [54]. The band structure and density of states were also calculated by DFT (Fig. S12). Bandgap value of Ag$_3$PO$_4$-C and 2 H-MoS$_2$ is 2.12 eV and 1.78 eV, respectively.

In Fig. 4f, the simulated charge density isosurface at the heterojunction interface between Ag$_3$PO$_4$-C and MoS$_2$ indicates electrons transfer from Ag$_3$PO$_4$-C to MoS$_2$ [55]. The hypothesized photocatalytic mechanism and potential transfer behavior of photogenerated carriers are based on free radicals trapping and bandgap structure analysis (Fig. 4g). If AM is a typical Type II heterojunction, as the diagram on the left shows, the potential differences will power h^+ in Ag$_3$PO$_4$-C VB migrate to 1 T&2 H-MoS$_2$ VB, and e$^-$ in CB of 1 T&2 H-MoS$_2$ migrate to Ag$_3$PO$_4$-C CB. As a result, the photogenerated charges will have lower redox capabilities. Both •OH and •O$_2^-$ cannot be created because neither the hole potential in 1 T&2 H-MoS$_2$ VB or the reduction potential of accumulated electrons in Ag$_3$PO$_4$-C CB are sufficient to oxidize H$_2$O to •OH or reduce O$_2$ to •O$_2^-$, and no EPR signal will be detectable. This hypothesis goes against the actual results in Fig. 4b and c. Therefore, the AM is not a typical Type II heterojunction, but has a direct Z-scheme construction. As the diagram in Fig. 4g on the right depicts, the

photogenerated holes in 1 T&2 H-MoS$_2$ VB and electrons in Ag$_3$PO$_4$-C CB will recombine, leaving holes in Ag$_3$PO$_4$-C VB and electrons in 1 T&2 H-MoS$_2$ CB independently. The potential for 1 T&2 H-MoS$_2$ CB is − 0.49 eV, which is more negative than the redox potential of •O$_2^-$/O$_2$ (−0.28 eV). Ag$_3$PO$_4$-C VB has holes with a potential of 2.43 eV, higher than the redox potential of •OH/H$_2$O (2.27 eV). Namely, the holes in Ag$_3$PO$_4$-C VB can boost the production of •OH. All in all, the theoretical calculation and experimental results show that the Z-scheme is successfully constructed, which can benefit the photocatalytic hydrogen recovery by purifying antibiotics wastewater due to the powerful oxidation and reduction ability [56].

3.5. Photocatalytic performance, mechanism discussion and degradation pathway for hydrogen recovery from antibiotics removal

The photocatalytic hydrogen recovery from characteristic antibiotics wastewater over AM-13 was evaluated from the water containing ciprofloxacin (CIP), tetracycline hydrochloride (TC), ofloxacin (OFL) and norfloxacin (NOR) (Fig. 5a). The H$_2$ yield increases with prolonged irradiation time and the highest H$_2$ amount is produced from CIP degradation after 2 h [57]. The H$_2$ yields and degradation efficiency of antibiotics are 105.88 μmol·g^{-1} and 84.79% for CIP, 48.22 μmol·g^{-1} and 65.81% for TC, 98.16 μmol·g^{-1} and 79.44% for OFL, and 108.02 μmol·g^{-1} and 88.36% for NOR, accordingly (Fig. 5b). The hydrogen recovery rate for these four antibiotics is ordered in NOR > CIP > OFL > TC. Besides, the TOC removal efficiency is 48.91% for CIP, 18.76% for TC, 44.67% for OFL and 47.11% for NOR, respectively (Fig. S13). The molecular structure diagram and the responding relative molecular mass are shown in Fig. S14. The relative molecular mass of these four antibiotics is: NOR (320) < CIP (332) < OFL (362) < TC (445). It is hard to degrade the antibiotics molecular with higher relative molecular mass compared to the smaller ones from the degradation efficiency and TOC removal efficiency. The H$_2$ yield shows a positive relevant relationship with the degradation efficiency of antibiotics wastewater. The higher degradation degree of the antibiotic, the higher the H$_2$ yield.

In the process of antibiotics degradation, antibiotics act as H donor and electron donor simultaneously. The actual H$_2$ storage capacity in theory for the antibiotic molecular depends on the molecular weight under the certain concentration. Theoretical hydrogen storage includes the detected H$_2$, donated dissociative H$^+$, adsorbed H and attached H$_2$ bubble in the real reaction of antibiotics degradation with simultaneous H$_2$ recovery. The favorable evidence is collected from the pH change before and after reaction (Fig. S15). The calculation process of hydrogen recovery rate (R(H)) is described in Text S1. The NOR possesses the most hydrogen storage capacity in theory (Table S1), which corresponds to the best H$_2$ accumulation performance. In Fig. 5c, the R(H) from CIP, TC, OFL and NOR is 86.32%, 69.57%, 89.09% and 84.93%, respectively, with the OFL solution showing the optimal R(H). R (H) can be as the reference for the H$_2$ energy regeneration efficiency from wastes recycling.

The mechanism of the photocatalytic hydrogen recovery from antibiotics wastewater can be further illustrated from the bandgap matching principle. As Fig. 5d depicts, frontier electrons densities of the lowest molecule occupies the orbital (LUMO) and the highest molecule occupies the orbital (HOMO) of CIP, TC, OFL and NOR. The intensity of the LUMO energy level decides the donated capacity of injecting electrons. The LUMO levels of CIP, TC, OFL and NOR are − 0.73, − 0.7, − 0.75 and − 0.92 eV, respectively [58], suggesting that NOR hold the highest potential energy of electron injection. Energy band illustration of AM photocatalyst system and four antibiotics are shown in Fig. 5e. NOR has the best ability to donate electrons to AM photocatalyst, which presents the best H$_2$ production performance. In contrast, TC with the lowest LUMO level presents the unsatisfied H$_2$ recovery. Band matching principle between the photocatalyst and the antibiotics can be used to evaluate the H$_2$ production activity and amount from antibiotics wastewater.
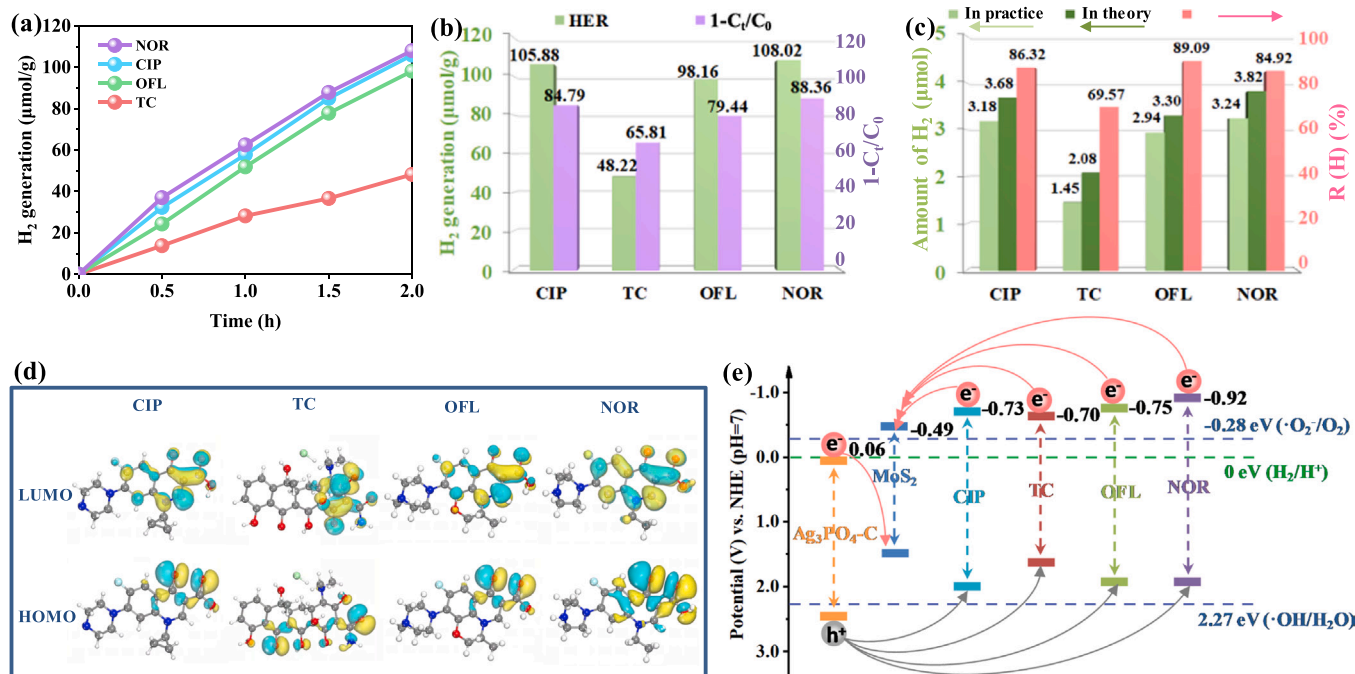
Fig. 5. The photocatalytic hydrogen recovery from typical antibiotics wastewater over AM-13 (antibiotics concentration: 10 mg/L, catalyst: 30 mg): (a) H_2 yield in 2 h, (b) Simultaneous H_2 production and antibiotics degradation efficiency after 2 h. (c) Actual H_2 yield and theoretical H_2 yield from different antibiotics, and the responding hydrogen recovery ratio (R(H), %). (d) Frontier electron densities of LUMO and HOMO of CIP, TC, OFL and NOR. (e) Energy band illustration of Ag_3PO_4-C, MoS_2, CIP, TC, OFL and NOR.

Atom	Charge(0) (c/Å³)	Charge(+1) (c/Å³)	Charge(−1) (c/Å³)	f0
C1	0.028	0.027	0.029	−0.001
C2	0.054	0.053	0.056	−0.0015
C3	0.023	0.021	0.025	−0.002
C4	0.033	0.012	0.055	−0.0215
C5	0.043	0.056	0.029	0.0135
C6	0.051	0.050	0.051	−0.0005
N1	0.009	0.017	0.000	0.0085
C7	0.087	0.156	0.018	0.069
C8	0.020	0.028	0.013	0.0075
C9	0.044	0.063	0.025	0.019
N2	0.058	0.012	0.104	−0.046
C10	−0.015	−0.007	−0.022	0.0075
C11	−0.007	−0.002	−0.012	0.005
N3	0.020	0.002	0.039	−0.0185
C12	−0.007	−0.002	−0.012	0.005
C13	−0.012	−0.005	−0.020	0.0075
C14	−0.012	−0.015	−0.009	−0.003
C15	−0.003	−0.001	−0.006	0.0025
C16	0.001	−0.001	0.003	−0.002
F1	0.027	0.026	0.029	−0.0015
O1	0.061	0.074	0.049	0.0125
C17	0.030	0.048	0.012	0.018
O2	0.034	0.053	0.014	0.0195
O3	0.011	0.017	0.006	0.0055
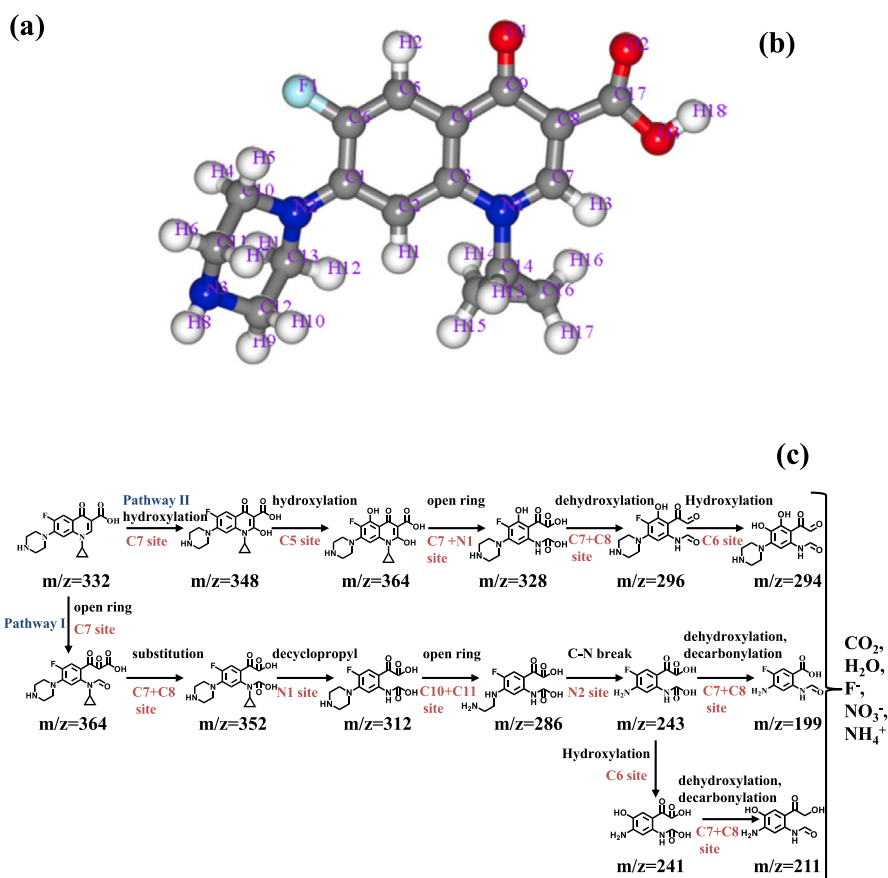
Fig. 6. (a) Fukui index of CIP (NPA charge distribution for 0, +1, −1,) and (b) the responding optimized molecular configuration. (c) Pathway and main intermediates during CIP degradation process with simultaneous hydrogen production.

It is important to forecast and assess the CIP degradation pathway with simultaneous hydrogen recovery from the theoretical prediction and experimental verification. It is also crucial to determine whether CIP molecule structure are more susceptible for electrophilic or nucleophilic attack in the degradation process. The Fukui index (f^0) is frequently applied to examine reactive sites under free radical assaults from conceptual density general function theory based on Natural population analysis (NPA) charge, related method is described in Text S2 [59]. The results of the computation of the Fukui indices about NPA charge are shown in Fig. 6a. The higher f^0 value of the site, the higher proclivity for attack by free radicals [60]. It is obvious that the C7, N1, O2 and F1 are the most active sites (corresponding to the molecular structure in Fig. 6b), with high f^0 values of 0.069, 0.0085, 00195 and -0.0015, respectively. As illustrated in Fig. 6c, the pathways of CIP degradation with simultaneous hydrogen recovery were proposed by combining Fukui index and main intermediates identification from mass spectrometry (MS) spectra (in Fig. S16). Finally, two pathways are presented in the following.

Pathway I: The C7 site is attacked firstly to obtain the intermediate product ($m/z = 364$), which is consistent with the calculation of Fukui index. Then the C7 site continues to be attacked, and the C8 site is hydroxylated to obtain the intermediate product ($m/z = 352$). The N1 site with the highest f^0 value among the N sites, is the next target, and the intermediate product ($m/z = 312$) is obtained by decyclopropylation. The intermediate product ($m/z = 286$) is obtained by ring opening at the C10 and C11 sites. The intermediate product ($m/z = 243$) is obtained by breaking the C-N bond at the N2 site. The intermediate product ($m/z = 199$) is obtained by dehydroxylation and hydroxylation at the C7 and C8 sites, respectively.

Pathway II: The C7 site is attacked firstly to produce the intermediate ($m/z = 348$). Hydroxylation of C5 site obtains the intermediate ($m/z = 364$). Oxidation of C7 and N1 sites produce the intermediate ($m/z = 328$). Dehydroxylation at C7 and C8 sites creates the intermediate product ($m/z = 296$). Hydroxylation of F at C6 site gives the intermediate product ($m/z = 294$). The final products CO_2, H_2O, F^-, NO_3^- and NH_4^+ are generated due to the further oxidation of intermediates. The pathway I may be the practical degradation pathway of CIP by generalized analysis of intermediates intensities ($m/z = 199$) in MS spectra. The f^0 values and the possible degradation pathways for TC, OFL and NOR were shown and described in Fig. S17–19. After generalized analyzing degradation pathway of four antibiotics, H protons can be donated in the process of decyclopropylaton, dihydroxylation and

demethylation.

3.6. Schematic illustration for photocatalytic hydrogen recovery from antibiotics wastewater

Schematic illustration for photocatalytic hydrogen recovery from the antibiotics over Z-scheme Ag$_3$PO$_4$ @MoS$_2$ based on the theoretical prediction and experimental data is illustrated in Fig. 7. Under photoexcitation, the electrons of Ag$_3$PO$_4$-C and MoS$_2$ can be excited from VB to CB. The Ag$_3$PO$_4$-C surface is confined with rich Vo, which act as interfacial recombination sites of Z-scheme Ag$_3$PO$_4$ @MoS$_2$, maintaining the powerful redox ability. It not only avoids charge consumption at the electron mediator, but also induces the MoS$_2$ distortion to be 1 T&2 H mixed phase, displaying enhanced hydrogen evolution activity compared with 2 H-MoS$_2$. At pH = 7, the redox potentials of $\bullet O_2^-/O_2$ and $\bullet OH/H_2O$ are -0.28, and 2.27 eV respectively [61]. The electrons in 2 H-MoS$_2$ CB have a potential of -0.49 eV, which is more negative than the redox potential of $\bullet O_2^-/O_2$ and can produce $\bullet O_2^-$. Ag$_3$PO$_4$-C VB possesses holes with a potential of 2.43 eV, which can oxidize -OH to produce $\bullet OH$ because it has a higher positive redox potential than that of $\bullet OH/H_2O$. In the process of antibiotics degradation, antibiotics not only act as H donors but also inject electrons to photocatalyst system. Finally, appreciable hydrogen energy is recovered from photocatalytic antibiotics degradation over the Ag$_3$PO$_4$ @MoS$_2$ photocatalyst system with high activity and stability.

4. Conclusion

In this work, a novel and exclusive composite, Z-scheme Ag$_3$PO$_4$ @MoS$_2$, was created by homogeneously immobilizing MoS$_2$ nanosheets on the surface of Ag$_3$PO$_4$ cubes with abundant oxygen vacancies. Vo promotes the generation and stabilization of 1 T-MoS$_2$, and it acts as electron mediator to accelerate the separation of photogenerated carriers, allowing electrons and holes with powerful oxidation and reduction ability. The degradation efficiency of CIP over optimized Ag$_3$PO$_4$ @MoS$_2$ is 91.7%. The photocatalytic hydrogen recovery from CIP, TC, OFL and NOR over optimized Ag$_3$PO$_4$ @MoS$_2$ composite were investigated (the highest performance is from NOR purifying: 54.01 $\mu mol \cdot g^{-1} \cdot h^{-1}$ H$_2$ production with 88.36% degradation efficiency). The degradation pathways of antibiotics are distinguished and confirmed by Fukui index prediction and MS spectra identification. H protons are donated in the process of decyclopropylaton and dihydroxylation for
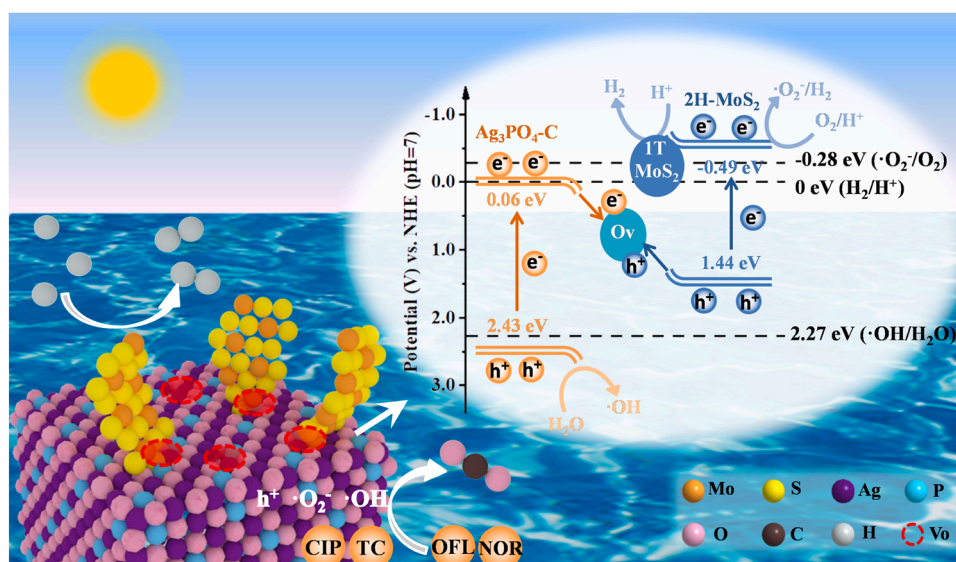

Fig. 7. Schematic illustration for photocatalytic hydrogen recovery from the antibiotics over Z-scheme Ag$_3$PO$_4$ @MoS$_2$ system.

antibiotics. This study figures out the new application direction of Ag_3PO_4 @MoS_2 photocatalysts and highlights the influence of Vo on stabilizing and activating 1 T phase MoS_2.

CRediT authorship contribution statement

Shuqu Zhang: Investigation, Writing – original draft, Writing – review & editing, Funding acquisition, Project administration. **Guanghua Hu:** Methodology, Writing – original draft, Investigation. **Meixue Chen:** Investigation. **Bing Li:** Supervision, Validation. **Weili Dai:** Supervision, Validation. **Fang Deng:** Supervision, Validation, **Lixia Yang:** Supervision, Validation, Funding acquisition. **Jianping Zou:** Supervision, Validation, **Shenglian Luo:** Funding acquisition, Supervision, Validation.

Declaration of Competing Interest

The authors declare that they have no known competing financial interests or personal relationships that could have appeared to influence the work reported in this paper.

Data availability

No data was used for the research described in the article.

Acknowledgments

Appendix A. Supporting information

Supplementary data associated with this article can be found in the online version at doi:10.1016/j.apcatb.2023.122584.

References

[1] J.C. Li, L. Zhao, M.B. Feng, C.H. Huang, P.Z. Sun, Abiotic transformation and ecotoxicity change of sulfonamide antibiotics in environmental and water treatment processes: a critical review, Water Res. 202 (2021), 117463, https://doi.org/10.1016/j.watres.2021.117463.

[2] L.K. Nagy, M. Abolhassani, S.I.P. Bakovic, Z. Anari, J.P. Moore II, B.G. Pollet, L. F. Greenlee, Electroless production of fertilizer (Struvite) and hydrogen from synthetic agricultural wastewaters, J. Am. Chem. Soc. 142 (2020) 18844–18858, https://doi.org/10.1021/jacs.0c07916.

[3] D.F. Yan, C. Mebrahtu, S.Y. Wang, R. Palkovits, Innovative electrochemical strategies for hydrogen production: From electricity input to electricity output, Angew. Chem. Int. Ed. (2022), https://doi.org/10.1002/ange.202214333.

[4] H.H. Ou, G.S. Li, W. Ren, B.J. Pan, G.H. Luo, Z.F. Hu, D.S. Wang, Y.D. Li, Atomically dispersed Au-assisted C–C coupling on red phosphorus for CO_2 photoreduction to C_2H_6, J. Am. Chem. Soc. 144 (2022) 22075–22082, https://doi.org/10.1021/jacs.2c09424.

[5] H.H. Ou, S.B. Ning, P. Zhu, S.H. Chen, A.L. Han, Q. Kang, Z.F. Hu, J.H. Ye, D. S. Wang, Y.D. Li, Carbon nitride photocatalysts with integrated oxidation and reduction atomic active centers for improved CO_2 conversion, Angew. Chem. Int. Ed. 134 (2022), e202206579, https://doi.org/10.1002/ange.202206579.

[6] H. Wang, Y. Wu, M.B. Feng, W.G. Tu, T. Xiao, T. Xiong, H.X. Ang, X.Z. Yuan, J. W. Chew, Visible-light-driven removal of tetracycline antibiotics and reclamation of hydrogen energy from natural water matrices and wastewater by polymeric carbon nitride foam, Water Res 144 (2018) 215–225, https://doi.org/10.1016/j.watres.2018.07.025.

[7] J. Liu, Y. Liu, N.Y. Liu, Y.Z. Han, X. Zhang, H. Huang, Y. Lifshitz, S.T. Lee, J. Zhong, Z.H. Kang, Metal-free efficient photocatalyst for stable visible water splitting via a two-electron pathway, Science 347 (2015) 970–974, https://doi.org/10.1126/science.aaa3145.

[8] H.H. Ou, C. Tang, X.R. Chen, M. Zhou, X.C. Wang, Solvated electrons for photochemistry syntheses using conjugated carbon nitride polymers, ACS Catal. 9 (2019) 2949–2955, https://doi.org/10.1021/acscatal.9b00314.

[9] S.Q. Zhang, L.L. Wang, C.B. Liu, J.M. Luo, J. Crittenden, X. Liu, T. Cai, J.L. Yuan, Y. Pei, Y.T. Liu, Photocatalytic wastewater purification with simultaneous hydrogen production using MoS_2 QD-decorated hierarchical assembly of $ZnIn_2S_4$

[10] on reduced graphene oxide photocatalyst, Water Res 121 (2017) 11–19, https://doi.org/10.1016/j.watres.2017.05.013.

[10] S. Kampouri, T.N. Nguyen, M. Spodaryk, R.G. Palgrave, A. Züttel, B. Smit, K. C. Stylianou, Concurrent photocatalytic hydrogen generation and dye degradation using MIL-125-NH_2 under visible light irradiation, Adv. Funct. Mater. 28 (2018) 1806368, https://doi.org/10.1002/adfm.201806368.

[11] J.R. He, L.J. Hu, C.T. Shao, S.J. Jiang, C.Z. Sun, S.Q. Song, Photocatalytic H_2O overall splitting into H_2 bubbles by single atomic sulfur vacancy CdS with spin polarization electric field, ACS Nano 15 (2021) 18006–18013, https://doi.org/10.1021/acsnano.1c06524.

[12] H. Zeng, Z.H. Li, G.S. Li, X.Q. Cui, M.X. Jin, T.F. Xie, L.L. Liu, M.P. Jiang, X. Zhong, Y.W. Zhang, H. Zhang, K. k Ba, Z.K. Yan, Y. Wang, S.Y. Song, K.K. Huang, S. H. Feng, Interfacial engineering of TiO_2/Ti_3C_2 mxene/carbon nitride hybrids boosting charge transfer for efficient photocatalytic hydrogen evolution, Adv. Energy Mater. 12 (2022), 2102765, https://doi.org/10.1002/aenm.202102765.

[13] J.M. Luo, S.Q. Zhang, M. Sun, L.X. Yang, S.L. Luo, J.C. Crittenden, A critical review on energy conversion and environmental remediation of photocatalysts with remodeling crystal lattice, surface, and interface, ACS Nano 13 (2019) 9811–9840, https://doi.org/10.1021/acsnano.9b03649.

[14] S. Yoshino, A. Iwase, Y. Yamaguchi, T.M. Suzuki, T. Morikawa, A. Kudo, Photocatalytic CO_2 reduction using water as an electron donor under visible light irradiation by Z-Scheme and photoelectrochemical systems over $(CuGa)_{0.5}ZnS_2$ in the presence of basic additives, J. Am. Chem. Soc. 144 (2022) 2323–2332, https://doi.org/10.1021/jacs.1c12636.

[15] F.Y. Zhao, P.P. Wang, A. Ruff, V. Hartmann, S. Zacarias, I.A.C. Pereira, M. M. Nowaczyk, M. Rögner, F. Conzuelo, W. Schuhmann, A photosystem I monolayer with anisotropic electron flow enables Z-scheme like photosynthetic water splitting, Energy Environ. Sci. 12 (2019) 3133–3143, https://doi.org/10.1039/C9EE01901D.

[16] B.J. Ng, L.K. Putri, X.Y. Kong, Y.W. Teh, P. Pasbakhsh, S.P. Chai, Z-scheme photocatalytic systems for solar water splitting, Adv. Sci. 7 (2020), 1903171, https://doi.org/10.1002/advs.201903171.

[17] G.C. Zuo, Y.T. Wang, W.L. Teo, Q.M. Xian, Y.L. Zhao, Direct Z-scheme TiO_2–$ZnIn_2S_4$ nanoflowers for cocatalyst-free photocatalytic water splitting, Appl. Catal. B-Environ. 291 (2021), 120126, https://doi.org/10.1016/j.apcatb.2021.120126.

[18] Y. Lin, C.P. Yang, S.H. Wu, X. Li, Y.J. Chen, W.L. Yang, Construction of built-in electric field within silver phosphate photocatalyst for enhanced removal of recalcitrant organic pollutants, Adv. Funct. Mater. 30 (2020), 2002918, https://doi.org/10.1002/adfm.202002918.

[19] Y.P. Bi, S.X. Ouyang, N. Umezawa, J.Y. Cao, J.H. Ye, Facet effect of single-crystalline Ag_3PO_4 sub-microcrystals on photocatalytic properties, J. Am. Chem. Soc. 133 (2011) 6490–6492, https://doi.org/10.1021/ja2002132.

[20] F. Teng, Z.L. Liu, A. Zhang, M. Li, Photocatalytic performances of Ag_3PO_4 polypods for degradation of dye pollutant under natural indoor weak light irradiation, Environ. Sci. Technol. 49 (2015) 9489–9494, https://doi.org/10.1021/acs.est.5b00735.

[21] L.F. Ni, T. Wang, K.C. Wang, J. Ma, Y.Y. Wang, Novel control strategy for membrane biofouling by surface loading of aerobically and anaerobically applicable photocatalytic optical fibers based on a Z-Scheme heterostructure Zr-MOFs/rGO/Ag_3PO_4 photocatalyst, Environ. Sci. Technol. (2022), https://doi.org/10.1021/acs.est.1c08031.

[22] K. Chang, M. Li, T. Wang, S.X. Ouyang, P. Li, L. Liu, J.H. Ye, Drastic layer-number-dependent activity enhancement in photocatalytic H_2 evolution over $nMoS_2$/CdS (n $\geq$ 1) under visible light, Adv. Energy Mater. 5 (2015), 1402279, https://doi.org/10.1002/aenm.201402279.

[23] S. Li, Z.C. Zhao, D.F. Yu, J.Z. Zhao, Y.P. Su, Y. Liu, Y.H. Lin, W.S. Liu, H. Xu, Z. T. Zhang, Few-layer transition metal dichalcogenides (MoS_2, WS_2, and WSe_2) for water splitting and degradation of organic pollutants: understanding the piezocatalytic effect, Nano Energy 66 (2019), 104083, https://doi.org/10.1016/j.nanoen.2019.104083.

[24] K. Zhang, B.J. Jin, Y.J. Gao, S.L. Zhang, H. Shin, H.B. Zeng, J.H. Park, Aligned heterointerface-induced 1T-MoS_2 monolayer with near-ideal Gibbs Free for stable hydrogen evolution reaction, Small 15 (2019), 1804903, https://doi.org/10.1002/smll.201804903.

[25] Y.Y. Wu, X.T. Chen, J.C. Cao, Y.Q. Zhu, W.J. Yuan, Z.F. Hu, Z.M. Ao, G.W. Brudvig, F.H. Tian, J.C. Yu, C.H. Li, Photocatalytically recovering hydrogen energy from wastewater treatment using MoS_2@ TiO_2 with sulfur/oxygen dual-defect, Appl. Catal. B-Environ. 303 (2022), 120878, https://doi.org/10.1016/j.apcatb.2021.120878.

[26] D. Sun, D. Huang, H.Y. Wang, G.L. Xu, X.Y. Zhang, R. Zhang, Y.G. Tang, D.A. EI-Hady, W. Alshitari, A.S. AL-Bogami, K. Amine, M.H. Shao, 1T MoS_2 nanosheets with extraordinary sodium storage properties via thermal-driven ion intercalation assisted exfoliation of bulky MoS_2, Nano Energy 61 (2019) 361–369, https://doi.org/10.1016/j.nanoen.2019.04.063.

[27] H.N. He, X.L. Li, D. Huang, J.Y. Luan, S.L. Liu, W.K. Pang, D. Sun, Y.G. Tang, W. Z. Zhou, L.R. He, C.H. Zhang, H.Y. Wang, Z.P. Guo, Electron-injection-engineering induced phase transition toward stabilized 1T-MoS_2 with extraordinary sodium storage performance, ACS Nano 15 (2021) 8896–8906, https://doi.org/10.1021/acsnano.1c01518.

[28] G. Kresse, D. Joubert, From ultrasoft pseudopotentials to the projector augmented-wave method, Phys. Rev. B 59 (1999) 1758–1775, https://doi.org/10.1103/PhysRevB.59.1758.

[29] J.P. Perdew, K. Burke, M. Ernzerhof, Generalized gradient approximation made simple, Phys. Rev. Lett. 77 (1996) 3865–3868, https://doi.org/10.1103/PhysRevLett.77.3865.

[30] P.E. Blöchl, Projector augmented-wave method, Phys. Rev. B 50 (1994) 17953, https://doi.org/10.1103/PhysRevB.71.035109.

[31] D.J. Martin, N. Umezawa, X.W. Chen, J.H. Ye, J.W. Tang, Facet engineered Ag₃PO₄ for efficient water photooxidation, Energy Environ. Sci. 6 (2013) 3380–3386, https://doi.org/10.1039/C3EE42260G.

[32] S. Wang, D. Zhang, B. Li, C. Zhang, Z.G. Du, H.M. Yin, X.F. Bi, S.B. Yang, Ultrastable in-plane 1T–2H MoS₂ heterostructures for enhanced hydrogen evolution reaction, Adv. Energy Mater. 8 (2018), 1801345, https://doi.org/10.1002/aenm.201801345.

[33] Y.M. He, L.H. Zhang, B.T. Teng, M.H. Fan, New application of Z-Scheme Ag₃PO₄/g-C₃N₄ composite in converting CO₂ to fuel, Environ. Sci. Technol. 49 (2015) 649–656, https://doi.org/10.1021/es5046309.

[34] M.M. Li, P.F. Wang, Z.Z. Ji, Z.R. Zhou, Y.G. Xia, Y. Li, S.H. Zhan, Efficient photocatalytic oxygen activation by oxygen-vacancy-rich CeO₂-based heterojunctions: synergistic effect of photoexcited electrons transfer and oxygen chemisorption, Appl. Catal. B: Environ. 289 (2021), 120020, https://doi.org/10.1016/j.apcatb.2021.120020.

[35] X.B. Li, B.B. Kang, F. Dong, Z.Q. Zhang, X.D. Luo, L. Han, J.T. Huang, Z.J. Feng, Z. Chen, J.L. Xu, B.L. Peng, Z.L. Wang, Enhanced photocatalytic degradation and H₂/H₂O₂ production performance of S-pCN/WO₂.₇₂ S-scheme heterojunction with appropriate surface oxygen vacancies, Nano Energy 81 (2021), 105671, https://doi.org/10.1016/j.nanoen.2020.105671.

[36] D.F. Yan, C.F. Xia, W.J. Zhang, Q. Hu, C.X. He, B.Y. Xia, S.Y. Wang, Cation defect engineering of transition metal electrocatalysts for oxygen evolution reaction, Adv. Energy Mater. (2022), 2202317, https://doi.org/10.1002/aenm.202202317.

[37] C. Sun, L.L. Wang, W.W. Zhao, L.B. Xie, J. Wang, J.M. Li, B.X. Li, S.J. Liu, Z. C. Zhuang, Q. Zhao, Atomic-level design of active site on two-dimensional MoS₂ toward efficient hydrogen evolution: Experiment, theory, and artificial intelligence modeling, Adv. Funct. Mater. 32 (2022), 2206163, https://doi.org/10.1002/adfm.202206163.

[38] F. Guo, X.L. Huang, Z.H. Chen, H.J. Ren, M.Y. Li, L.Z. Chen, MoS₂ nanosheets anchored on porous ZnSnO₃ cubes as an efficient visible-light-driven composite photocatalyst for the degradation of tetracycline and mechanism insight, J. Hazard. Mater. 390 (2020), 122158, https://doi.org/10.1016/j.jhazmat.2020.122158.

[39] K.P. Dhakal, G. Ghimire, K. Chung, D.L. Duong, S.W. Kim, J. Kim, Probing multiphased transition in bulk MoS₂ by direct electron injection, ACS Nano 13 (2019) 14437–14446, https://doi.org/10.1021/acsnano.9b08037.

[40] Y.M. Zhang, X.Y. Yang, Y.L. Wang, P. Zhang, D. Liu, Y.W. Li, Z.Z. Jin, B.B. Mamba, A.T. Kuvarega, J.Z. Gui, Insight into l-cysteine-assisted growth of Cu₂S nanoparticles on exfoliated MoS₂ nanosheets for effective photoreduction removal of Cr (VI), Appl. Surf. Sci. 518 (2020), 146191, https://doi.org/10.1016/j.apsusc.2020.146191.

[41] S.J.R. Tan, S. Sarkar, X.X. Zhao, X. Luo, Y.Z. Luo, S.M. Poh, I. Abdelwahab, W. Zhou, T. Venkatesan, W. Chen, S.Y. Quek, K.P. Loh, Temperature- and phase-dependent phonon renormalization in 1T'-MoS₂, ACS Nano 12 (2018) 5051–5058, https://doi.org/10.1021/acsnano.8b02649.

[42] W. Zhao, Y. Liu, Z.B. Wei, S.G. Yang, H. He, C. Sun, Fabrication of a novel p–n heterojunction photocatalyst n-BiVO₄@p-MoS₂ with core–shell structure and its excellent visible-light photocatalytic reduction and oxidation activities, Appl. Catal. B-Environ. 185 (2016) 242–252, https://doi.org/10.1016/j.apcatb.2015.12.023.

[43] Y. Hu, X.Q. Hao, Z.W. Cui, J. Zhou, S.Q. Chu, Y. Wang, Z.G. Zou, Enhanced photocarrier separation in conjugated polymer engineered CdS for direct Z-scheme photocatalytic hydrogen evolution, Appl. Catal. B-Environ. 260 (2020) 118131, https://doi.org/10.1016/j.apcatb.2019.118131.

[44] C. Cheng, B.W. He, J.J. Fan, B. Cheng, S.W. Cao, J.G. Yu, An inorganic/organic S-scheme heterojunction H₂-production photocatalyst and its charge transfer mechanism, Adv. Mater. 33 (2021), 2100317, https://doi.org/10.1002/adma.202100317.

[45] X. Li, J.D. Hu, T.Y. Yang, X.G. Yang, J.F. Qu, C.M. Li, Efficient photocatalytic H₂-evolution coupled with valuable furfural-production on exquisite 2D/2D LaVO₄/g-C₃N₄ heterostructure, Nano Energy 92 (2022), 106714, https://doi.org/10.1016/j.nanoen.2021.106714.

[46] T.M. Su, C.Z. Men, L.Y. Chen, B.X. Chu, X. Luo, H.B. Ji, J.H. Chen, Z.Z. Qin, Sulfur vacancy and Ti₃C₂Tₓ cocatalyst synergistically boosting interfacial charge transfer in 2D/2D Ti₃C₂Tₓ/ZnIn₂S₄ heterostructure for enhanced photocatalytic hydrogen evolution, Adv. Sci. 9 (2022), 2103715, https://doi.org/10.1002/advs.202103715.

[47] N.Y. Li, X.J. Chen, J. Wang, X.M. Liang, L.T. Ma, X.L. Jing, D.L. Chen, Z.Q. Li, ZnSe nanorods–CsSnCl₃ perovskite heterojunction composite for photocatalytic CO₂ reduction, ACS Nano 16 (2022) 3332–3340, https://doi.org/10.1021/acsnano.1c11442.

[48] Q. Xiao, T. Wang, S.L. Yu, P. Yi, L. Li, Influence of UV lamp, sulfur(IV) concentration, and pH on bromate degradation in UV/sulfite systems: Mechanisms and applications, Water Res 111 (2017) 288–296, https://doi.org/10.1016/j.watres.2017.01.018.

[49] C.Q. Tan, H. Zhao, X. Wang, H. Yu, S. Chong, Y. Xu, E.D. Du, M. Chen, X.M. Peng, L.H. Su, Feasibility of micropollutants removal by solar-activated persulfate: Reactive oxygen species formation and influence on DBPs, Water Res 210 (2022), 117981, https://doi.org/10.1016/j.watres.2021.117981.

[50] D. Escalera-López, Z.H. Lou, N.V. Rees, Benchmarking the activity, stability, and inherent electrochemistry of amorphous molybdenum sulfide for hydrogen production, Adv. Energy Mater. 9 (2019), 1802614, https://doi.org/10.1002/aenm.201802614.

[51] Y.H. Guo, N.C. Ramos, J.A. Clark, H.W. Hillhouse, Electrochemical oxidation of pharmaceuticals in synthetic fresh human urine: Using selective radical quenchers to reveal the dominant degradation pathways and the scavenging effects of individual urine constituents, Water Res (2022), 118722, https://doi.org/10.1016/j.watres.2022.118722.

[52] S.Q. Zhang, Z.F. Zhang, B. Li, W.L. Dai, Y.M. Si, L.X. Yang, S.L. Luo, Hierarchical Ag₃PO₄@ ZnIn₂S₄ nanoscoparium: an innovative Z-scheme photocatalyst for highly efficient and predictable tetracycline degradation, J. Colloid Interf. Sci. 586 (2021) 708–718, https://doi.org/10.1016/j.jcis.2020.10.140.

[53] P. Makula, M. Pacia, W. Macyk, How to correctly determine the band gap energy of modified semiconductor photocatalysts based on UV–Vis spectra, J. Phys. Chem. Lett. 9 (2018) 6814–6817, https://doi.org/10.1021/acs.jpclett.8b02892.

[54] M.X. Tan, Y. Ma, C.Y. Yu, Q.J. Luan, J.J. Li, C.B. Liu, W.J. Dong, Y.J. Su, L.J. Qiao, L. Gao, Q.P. Lu, Y. Bai, Boosting photocatalytic hydrogen production via interfacial engineering on 2D ultrathin Z-Scheme ZnIn₂S₄/g-C₃N₄ heterojunction, Adv. Funct. Mater. 32 (2022), 2111740, https://doi.org/10.1002/adfm.202111740.

[55] P.L. Wang, S.Y. Fan, X.Y. Li, J. Wang, Z.Y. Liu, C.P. Nai, M.O. Tadé, S.M. Liu, Piezotronic effect and hierarchical Z-scheme heterostructure stimulated photocatalytic H₂ evolution integrated with C-N coupling of benzylamine, Nano Energy 89 (2021), 106349, https://doi.org/10.1016/j.nanoen.2021.106349.

[56] T.S. Wang, S.H. Liu, Y.Y. Hu, Z.W. Xu, S.Y. Hu, G.Q. Li, J. Xu, M. Wang, J.H. Zhang, W. Yu, X. Ma, Liquid metal/wood anisotropic conductors for flexible and recyclable electronics, Adv. Mater. (2022), 2200172, https://doi.org/10.1002/admi.202200172.

[57] V.M. Daskalaki, M. Antoniadou, G.L. Puma, D.I. Kondarides, P. Lianos, Solar light-responsive Pt/CdS/TiO₂ photocatalysts for hydrogen production and simultaneous degradation of inorganic or organic sacrificial agents in wastewater, Environ. Sci. Technol. 44 (2010) 7200–7205, https://doi.org/10.1021/es9038962.

[58] X.H. Pang, W.J. Guo, W.H. Li, J.D. Xie, B.R. Hou, Electrochemical, quantum chemical and SEM investigation of the inhibiting effect and mechanism of ciprofloxacin, norfloxacin and ofloxacin on the corrosion for mild steel in hydrochloric acid, Sci. China Ser. B 51 (2008) 928–936, https://doi.org/10.1007/s11426-008-0099-z.

[59] J.Y. Guo, H.B. Sun, X.Z. Yuan, L.B. Jiang, Z.B. Wu, H.B. Yu, N. Tang, M.D. Yu, M. Yan, J. Liang, Photocatalytic degradation of persistent organic pollutants by Co-Cl bond reinforced CoAl-LDH/Bi₁₂O₁₇Cl₂ photocatalyst: mechanism and application prospect evaluation, Water Res 219 (2022), 118558, https://doi.org/10.1016/j.watres.2022.118558.

[60] S. Li, T.B. Huang, P.H. Du, W. Liu, J.Y. Hu, Photocatalytic transformation fate and toxicity of ciprofloxacin related to dissociation species: Experimental and theoretical evidences, Water Res 185 (2020), 116286, https://doi.org/10.1016/j.watres.2020.116286.

[61] T. Cai, Y.T. Liu, L.L. Wang, S.Q. Zhang, Y.X. Zeng, J.L. Yuan, J.H. Ma, W.Y. Dong, C.B. Liu, S.L. Luo, Silver phosphate-based Z-Scheme photocatalytic system with superior sunlight photocatalytic activities and anti-photocorrosion performance, Appl. Catal. B-Environ. 208 (2017) 1–13, https://doi.org/10.1016/j.apcatb.2017.02.065.